Patterned bilayer graphene as a tunable strongly correlated system

Z. E. Krix [*] and O. P. Sushkov

School of Physics, University of New South Wales, Sydney 2052, Australia
and Australian Research Council Centre of Excellence in Low-Energy Electronics Technologies,
University of New South Wales, Sydney 2052, Australia

Recent observations of superconductivity in moire graphene have led to an intense interest in that system, with subsequent studies revealing a more complex phase diagram including correlated insulators and ferromagnetic phases. Here we propose an alternate system, electrostatically patterned bilayer graphene, in which a supermodulation is induced via metallic gates rather than the moire effect. We show that, by varying either the gap or the modulation strength, bilayer graphene can be tuned into the strongly correlated regime. Further calculations show that this is not possible in monolayer graphene. We present a general technique for addressing Coulomb screening of the periodic potential and demonstrate that this system is experimentally feasible.

I. INTRODUCTION

Superconductivity in twisted bilayer graphene [1] occurs at a twist angle which turns the lowest-lying energy states into a flat band [2]. More generally, strongly correlated phases due to flat-band physics arise in a broad range of materials. Observations of superconductivity [1,3–6], correlated insulators [3–5,7–9], ferromagnetism [10,11] and nematic order [8,12,13] have been reported across the family of twisted graphene systems. This includes twisted bilayer graphene [1], twisted trilayer graphene [6], and twisted double-bilayer graphene [13]. Flat bands also arise in twisted transition metal dichalcogenides (TMDCs) [14] and kagome systems which exhibit superconductivity, ferromagnetism, and charge density waves [15–20].

Given the high level of interest in strongly correlated phases arising from flat-band systems, particularly twisted bilayer graphene, this work proposes an alternative graphene-based system which is fully tunable and contains a well-defined, isolated flat band. The system we consider is a graphene bilayer with no twist angle and a patterned electrostatic gate a vertical distance z from the bilayer. For brevity we refer to this system as patterned bilayer graphene (PBG). The guiding idea is to restructure the bare energy bands of bilayer graphene via periodic electrostatic gating rather than with a twist-induced moire superlattice. Conceptually, this is a continuation of our previous work on semiconductor artificial crystals [21], which are less efficient than PBG at generating a strong modulation. A major advantage of this approach is that it bypasses the issue of twist-angle disorder [22] (i.e., long-range spatial variation of the twist angle). The moire flat band occurs at a precise value of twist angle ($\theta \approx 1.1^\circ$) and a modest amount of twist disorder ($\lesssim 10\%$) can destroy this

band [23]. We demonstrate that PBG has no equivalent fine tuning or disorder problem.

The central advantage of our system is its controllability. A designed superlattice potential induced by patterned electrostatic gating can have any desired lattice symmetry (e.g., square, triangular, honeycomb [24], Lieb, or kagome) and lattice constants as small as 40 nm [25]. It is also possible to tune both the strength of the supermodulation and the particle density independently [25–27]. In contrast, moire graphene superlattices have a triangular symmetry which is fixed by the crystal structure of graphene. The superlattice constant $a \approx 13$ nm is also fixed by the flat-band condition $\theta \approx 1.1^\circ$. Tuning the superlattice strength is only possible by applying hydrostatic pressure [4,28], though in trilayer systems it may be possible to do this by varying the band gap [9]. Some prior works have focused on patterning monolayer graphene, either by etching holes directly into the graphene sheet [29] or by patterned electrostatic gating [25,30]. Reference [29] demonstrates, theoretically, that patterning introduces an energy gap in the graphene dispersion while Refs. [25,30] measure magnetotransport properties of a real device and show that the result of patterning is essentially a correction to single-particle physics. There is not, however, the possibility for generating an isolated flat band or strongly correlated phases in these monolayer graphene systems. Patterned bilayer graphene has also recently been studied theoretically with regards to its topological properties [31].

Our results are derived from band structure calculations in a continuum, bilayer graphene model with imposed superlattice potential. We find that bilayer graphene can be driven into the Mott regime by inducing a sufficiently strong band gap and potential modulation. This occurs because a flat band develops in the lowest-energy band of the PBG dispersion. By detuning either the band gap or potential modulation the system can be tuned out of the Mott regime while keeping the total electron density fixed. Within the flat band it is possible to mimic the dispersion of many different two-dimensional

---

*z.krix@unsw.edu.au

lattices including square, triangular, kagome, and Lieb, by varying the symmetry of the patterned gate. We show, using an analogous calculation, that it is not possible to generate a flat band in monolayer graphene. Lastly, we study electron-electron screening in bilayer graphene. Current techniques are not able to address a system with both an unbounded dispersion and a strong potential modulation; we develop a general technique to address Coulomb screening in this limit. The technique we develop is general and could also be applied to, for example, the problem of impurity screening in bilayer graphene. We show that screening of the periodic potential is strong but can be overcome by experimentally realistic gate voltages. Our results show that patterned bilayer graphene is an experimentally viable way to engineer an isolated flat with almost complete control over the underlying effective Hubbard model.

II. THEORETICAL TECHNIQUES

Our starting point is a plain bilayer graphene sheet with external, perpendicular electric field $\boldsymbol{E}$ inducing an energy gap Δ. The relationship between field and gap is roughly $|\boldsymbol{E}| \propto \Delta$, where the constant of proportionality is such that a displacement field of $1 \, \mathrm{Vn^{-1}m}$ leads to a gap $\Delta = 100 \, \mathrm{meV}$ [32]. We find that the value of the gap is important but does not need to be finely tuned, we discuss conditions on Δ below. The low-energy effective Hamiltonian for a single valley of bilayer graphene is [33]

$$H_{\mathrm{BLG}} = \begin{bmatrix} \Delta/2 & vp_- & 0 & \gamma \\ vp_+ & \Delta/2 & 0 & 0 \\ 0 & 0 & -\Delta/2 & vp_- \\ \gamma & 0 & vp_+ & -\Delta/2 \end{bmatrix}, \quad (1)$$

where $v \approx 1 \times 10^6 \, \mathrm{ms^{-1}}$ is the Fermi velocity of monolayer graphene, $\gamma \approx 0.38 \, \mathrm{eV}$ is the coupling between graphene layers, and the operator $p_\pm$ is defined by $p_\pm = p_x \pm ip_y$. These values are taken from Ref. [33]. The Hamiltonian is composed of 2×2 blocks. Each diagonal block is the Hamiltonian of a single graphene layer, and each layer has a different energy shift $\pm \Delta/2$ depending on its position in the external field. The off-diagonal blocks, which couple the two layers, arise from the simplest kind of interlayer hopping, between two carbon atoms which are vertically aligned: γ is the matrix element for this hopping.

One can also include terms in the Hamiltonian which describe longer-range interlayer hopping (these are denoted by γ_3 and γ_4 in Ref. [33]). As discussed in Ref. [33] they contribute to trigonal warping and particle-antiparticle asymmetry of the band dispersion. These additional terms are secondary to the major terms v and γ, and, for the sake of physical transparency, we neglect them here.

In the limit $|\varepsilon| \ll \gamma$, the two low-energy bands which arise from Eq. (1) are roughly quadratic: $\varepsilon(p) = \pm \sqrt{(p^2/2m^*)^2 + \Delta^2/4}$, where the effective mass is $m^* = \gamma/2v^2 \approx 0.03m_e$.

Over the top of this Hamiltonian we wish to introduce a spatially modulated electrostatic potential $U(\boldsymbol{r})$, due to patterned gating. Suppose, first, that the periodic potential
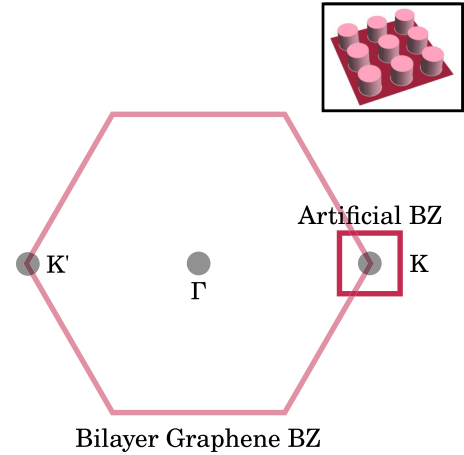
FIG. 1. Sketch of the two Brillouin zones. The larger is that of the underlying bilayer graphene system and the smaller is that of the artificial crystal. Since we use an expansion about the K points of the bilayer graphene BZ, the artificial BZ is centered at a K point. The inset shows the artificial crystal in real space.

defined *at the gate* is given by

$$U_{\mathrm{gate}}(\boldsymbol{r}) = W \sum_{\boldsymbol{G}} e^{i\boldsymbol{G} \cdot \boldsymbol{r}} U_{\boldsymbol{G}},$$

where the vectors $\boldsymbol{G}$ are the reciprocal lattice vectors of the artificial superlattice and W is a parameter taking dimensions of energy which controls the strength of the superlattice. In our calculation, the dimensionless parameters $U_{\boldsymbol{G}}$ define a muffin-tin shaped, periodic potential with square-lattice symmetry (see the inset to Fig. 1). In this case W is equal to the total variation in potential energy from minimum to maximum, the "height" of the muffin tin. For concreteness we study $W > 0$, which corresponds to an array of antidots. The opposite limit $W < 0$ is very similar and we discuss this below. The potential $U(\boldsymbol{r})$ at the plane of the bilayer graphene sheet is then

$$U(\boldsymbol{r}) = W \sum_{\boldsymbol{G}} e^{i\boldsymbol{G} \cdot \boldsymbol{r}} e^{-Gz} U_{\boldsymbol{G}}, \quad (2)$$

where z is the vertical distance between the patterned gate and the bilayer. This exponential suppression of the higher harmonics follows directly from Poisson's equation. For a square lattice, the first harmonic has $G = g = 2\pi/a$, where a is the superlattice period. We choose parameters $a = 80 \, \mathrm{nm}$ and $z = 10 \, \mathrm{nm}$ which are reasonable from an experimental standpoint. The suppression of the second harmonic relative to the first is then $e^{-gz} \sim 0.5$ meaning that higher harmonics should not be neglected. For a smaller lattice constant, $a = 40 \, \mathrm{nm}$, $e^{-gz} \sim 0.2$ and so higher harmonics are slightly less significant. Given this periodic potential the total Hamiltonian becomes

$$H_{\mathrm{PBG}} = H_{\mathrm{BLG}} + U(\boldsymbol{r}).$$

The matrix structure of $U(\boldsymbol{r})$ is trivial, it is a 4×4 identity matrix. Strictly speaking there should also be a spatially varying correction to the gap Δ due to each graphene layer being a slightly different distance from the patterned gate. This correction, however, produces a small effect relative to the major

contribution $U(\mathbf{r})$, and can be neglected. Note that the applied, constant field (which induces Δ) will give a similar, diagonal contribution to the Hamiltonian. Since that contribution is spatially invariant, it simply shifts all energy levels by the same amount, and can be left out of the Hamiltonian.

Since the artificial superlattice period a is larger than the period of the graphene lattice and since we are focusing on a single valley, our approach amounts to defining a smaller, artificial Brillouin zone (either square or hexagonal) around one of the vertices of the original bilayer graphene Brillouin zone. This is sketched in Fig. 1.

The energy levels of the Hamiltonian H_{PBG} can be obtained exactly by numerical diagonalization. We must first compute the matrix elements of H_{PBG} in a particular basis. For simplicity, we choose basis vectors $|\mathbf{k} + \mathbf{G}, i\rangle$, defined by

$$|\mathbf{k} + \mathbf{G}, i\rangle = \frac{1}{\sqrt{A}} e^{i(\mathbf{k}+\mathbf{G})\cdot\mathbf{r}} |i\rangle,$$

$$(|i\rangle)_j = \delta_{ij}, \quad i, j = 1, \ldots, 4.$$

Here $|i\rangle$ is a 4-tuple, $\mathbf{G}$ is a reciprocal lattice vector of the superlattice, and $\mathbf{k}$ is the quasimomentum, which sits somewhere within the *artificial* Brillouin zone. The normalization factor A is just the total area of the sample. For example, at $i = 1$, we have

$$|1\rangle = \begin{bmatrix} 1 \\ 0 \\ 0 \\ 0 \end{bmatrix}.$$

The matrix elements of H_{PBG} are then

$$\langle \mathbf{k} + \mathbf{G}, i | H_{\mathrm{PBG}} | \mathbf{k} + \mathbf{G}', j \rangle = \langle i | H_{\mathrm{BLG}}(\mathbf{k} + \mathbf{G}) | j \rangle \delta_{\mathbf{G},\mathbf{G}'}$$
$$+ \delta_{i,j} W U_{\mathbf{G}-\mathbf{G}'} e^{-|\mathbf{G}-\mathbf{G}'|z}.$$

In $H_{\mathrm{BLG}}(\mathbf{k})$ the operator $p_{\pm}$ is replaced by the complex number $k_{\pm} = k_x \pm i k_y$. The matrix elements of the potential are given by

$$U_{\mathbf{G}} = 2\pi \frac{R^2}{A_{\mathrm{cell}}} \frac{J_1(|\mathbf{G}|R)}{|\mathbf{G}|R},$$

where R is the radius of a single antidot, taken to be $R = 15\,\mathrm{nm}$ in our calculations, and A_{cell} is the unit-cell area of the artificial crystal; J_1 is a Bessel function of the first kind. The only differences between square and triangular lattices are the choice of reciprocal lattice vectors $\mathbf{G}$ and the size of A_{cell} in the above equation. To diagonalize this Hamiltonian numerically we must make the set of basis vectors finite by choosing a maximal $\mathbf{G}$ vector. In practice, we simply increase the size of the basis until the energy levels or eigenvectors converge. The result of this procedure is a set of energy levels $\varepsilon_n(\mathbf{k})$ and eigenvectors $\psi_{n,\mathbf{k}}(\mathbf{r})$, each being a function of the quasimomentum $\mathbf{k}$ of the artificial superlattice. The band index can take values $n = \pm 1, \pm 2, \ldots$ with the charge neutrality point occurring between $n = -1$ and $+1$. Each band n is degenerate across valleys and spins and contains a number of particles, $n_0 = 4/A_{\mathrm{cell}}$, corresponding to complete filling of one artificial Brillouin zone (accounting for spin and valley degeneracy). At $a = 80\,\mathrm{nm}$ we have $n_0 = 6.25 \times 10^{10}\,\mathrm{cm}^{-2}$, while at $a = 40\,\mathrm{nm}$ we have $n_0 = 2.5 \times 10^{11}\,\mathrm{cm}^{-2}$.

The parameter W has been defined at the patterned gate. This allows us to fairly compare the strength of a square lattice with that of a kagome lattice (for example). Still, it is useful to have a general idea of the amplitude of the potential at the two-dimensional electron gas (2DEG). Looking at the first harmonic only, this quantity is

$$W_{\mathrm{2DEG}} = W 2\pi \frac{R^2}{A_{\mathrm{cell}}} \frac{J_1(|\mathbf{G}|R)}{|\mathbf{G}|R} e^{-|\mathbf{G}|z}.$$

As a rough approximation, keeping only first harmonics, the potential at the 2DEG is $2W_{\mathrm{2DEG}}[\cos(gx) + \cos(gy)]$. For the parameters we are using the conversion is $W_{\mathrm{2DEG}} = 0.042W$. At $W = 30\,\mathrm{meV}$ we have $W_{\mathrm{2DEG}} = 1.26\,\mathrm{meV}$. If the total variation in potential energy is $30\,\mathrm{meV}$ at the gate, then the equivalent quantity at the 2DEG is around $8W_{\mathrm{2DEG}} = 10\,\mathrm{meV}$.

III. GENERATING A FLAT BAND

We will first demonstrate how the band structure evolves as W is tuned, keeping the band gap fixed at $\Delta = 15\,\mathrm{meV}$. Our results are summarized in Fig. 2. In the first panel of Fig. 2, $W = 0$ and the dispersion is just the result of bandfolding the bare BLG dispersion into the artificial, square Brillouin zone: at Γ the electron band starts at $+7.5\,\mathrm{meV}$ and the hole band starts at $-7.5\,\mathrm{meV}$. We find that as the potential is turned on the first hole band ($n = -1$) is separated from the remaining hole bands ($n = -2, -3, \ldots$) and develops a total bandwidth $\delta_b = 0.53\,\mathrm{meV}$, which does not change as W is increased beyond $30\,\mathrm{meV}$. The existence of this flat band is the main focus of our work. As can be seen, the full dispersion is electron-hole asymmetric; we address this point later in the section.

To study the flat band more closely, we plot it individually in Fig. 3 for a range of W values. We find that the effect of the potential is not only to separate this band, but to transform its dispersion into that of a tight-binding model on a square lattice with nearest-neighbor hopping (green band in Fig. 3). This dispersion is $2t[\cos(ak_x) + \cos(ak_y)]$ where t is the matrix element for nearest-neighbor hopping. We can thus map the physics of the flat band to an effective tight-binding model by equating the total bandwidth δ_b with $8t$: we find that the effective hopping parameter is $t = 0.066\,\mathrm{meV}$. The number of states within this band is $n_0 = 4/A_{\mathrm{cell}} = 6.25 \times 10^{10}\,\mathrm{cm}^{-2}$, with the factor 4 arising from spin and valley degeneracy.

The emergence of a flat band is related to the energy gap. A plain bilayer graphene sheet has two, roughly quadratic bands with opposite curvature and the effect of an out-of-plane electric field is not only to open a gap between these bands, but to flatten the bottom of each band as well. The idea, then, is to first flatten the bottom of the band using a constant electric field and then to separate a flat band by imposing a periodic modulation. The artificial Brillouin zone "cuts out" the flat part of the hole band. We thus require that the first Brillouin zone of the artificial lattice fit within the flattened part of the bare BLG dispersion. To generate a flat band using a smaller superlattice period, that is, with a larger Brillouin zone, we must increase the size of the flat region in the bare BLG dispersion by increasing the gap. The presence of the gap makes it easier for an external potential to localize electrons,

W = 0 meV

W = 15 meV

Artificial
BZ
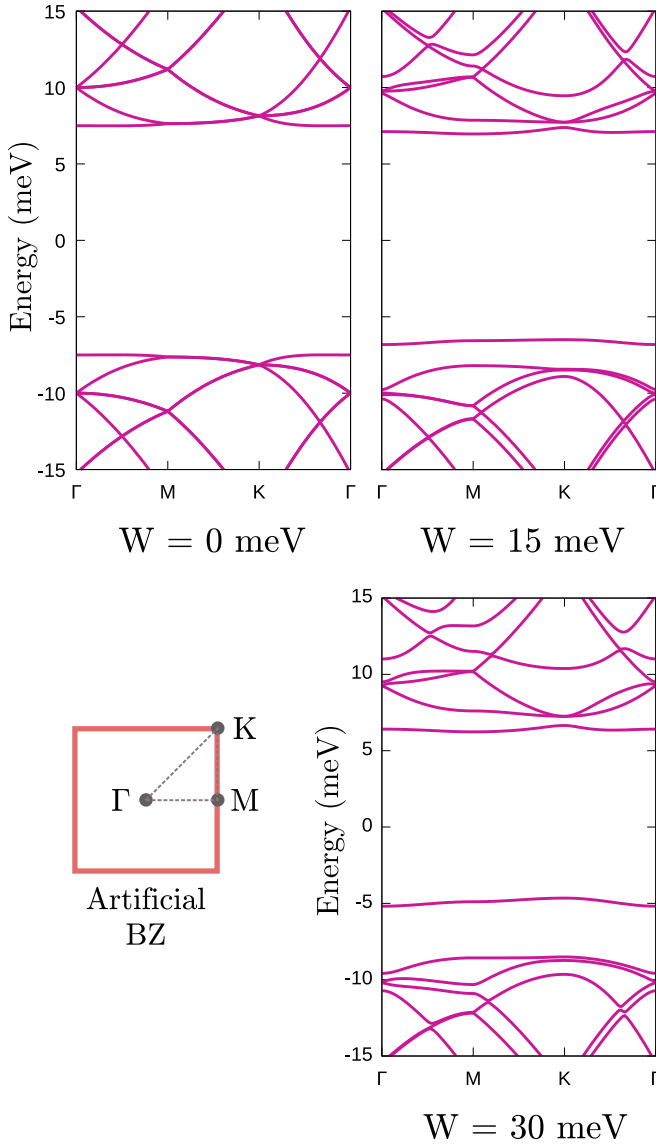
W = 30 meV

FIG. 2. Evolution of dispersion from $W = 0$ to 30 meV. In each panel $a = 80$ nm, $\Delta = 15$ meV, $R = 15$ nm, and $z = 10$ nm. At $W = 0$ meV we have the bare BLG dispersion bandfolded into the artificial Brillouin zone. By $W = 30$ meV a single, flat band (width ≈ 0.5 meV) has separated from the rest of the hole bands. Points around the artificial Brillouin zone are defined in the inset.

and also allows for separation between electron and hole bands so that the resulting flat band is isolated.

This suggests a criterion for the minimum band gap Δ which can give a flat band. If we approximate the bare dispersion by $\varepsilon(k) = \sqrt{(p^2/2m^*)^2 + \Delta^2/4}$ then the "flat region" of the dispersion is roughly defined by $p^2/m^* = \Delta$. If we want the boundary of this region to coincide with the Brillouin zone boundary then the condition on the band gap is $\Delta \sim (\pi/a)^2/m^* = 3.5$ meV.

To demonstrate the importance of the band gap we compute the evolution of the band structure as Δ is tuned, keeping $W = 30$ meV fixed. The results are plotted in Fig. 4. At $\Delta = 0$ the electron and hole bands touch and there is no isolated flat band. At $\Delta = 5$ meV the $n = -1$ band becomes
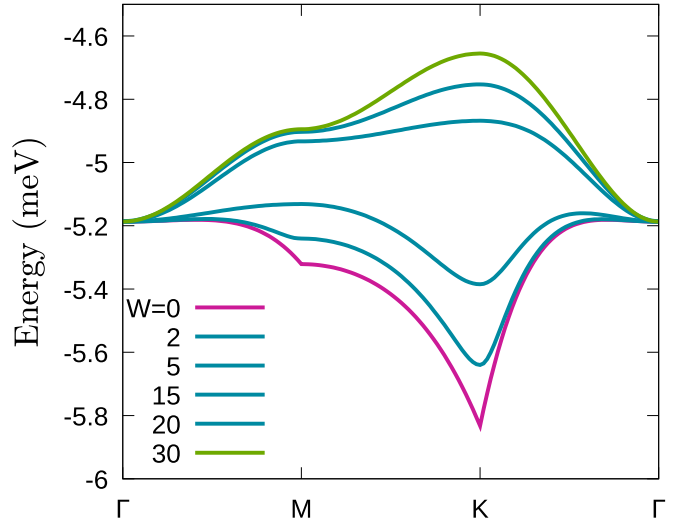
FIG. 3. Zoom-in of the $n = -1$ band in Fig. 2. Each curve corresponds to a different value of W, with $W = 0$ meV for the lowest curve and $W = 30$ meV for the uppermost curve.

isolated. And, finally, at $\Delta = 15$ meV (Fig. 2), the dispersion of the $n = -1$ band matches that of the square-lattice tight-binding model: $2t[\cos(k_x a) + \cos(k_y a)]$. Bilayer graphene can be tuned in and out of the flat-band regime in two ways. First, one can fix the band gap and increase the potential modulation from zero. Second, one can fix the potential modulation and increase the gap.

The shape of the flat-band dispersion follows from shape of the potential energy: a square array of hat functions. We have defined the potential such that electrons in the upper BLG band ($n > 0$) minimize their energy at minimal values of $U(r)$. Electrons in the lower BLG band thus minimize their energy by seeking the potential maxima, and can be localized
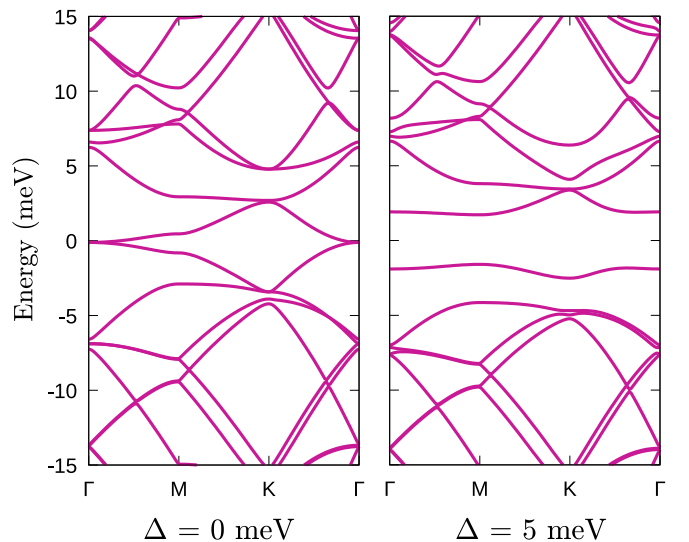
$\Delta = 0$ meV

$\Delta = 5$ meV

FIG. 4. Evolution of dispersion from $\Delta = 0$ to 5 meV. In each panel $a = 80$ nm, $W = 30$ meV, $R = 15$ nm, and $z = 10$ nm. The flat band becomes isolated by $\Delta = 5$ meV, but the dispersion $2t[\cos(k_x a) + \cos(k_y a)]$ does not develop until $\Delta = 15$ meV (Fig. 2).

(a)

(b)
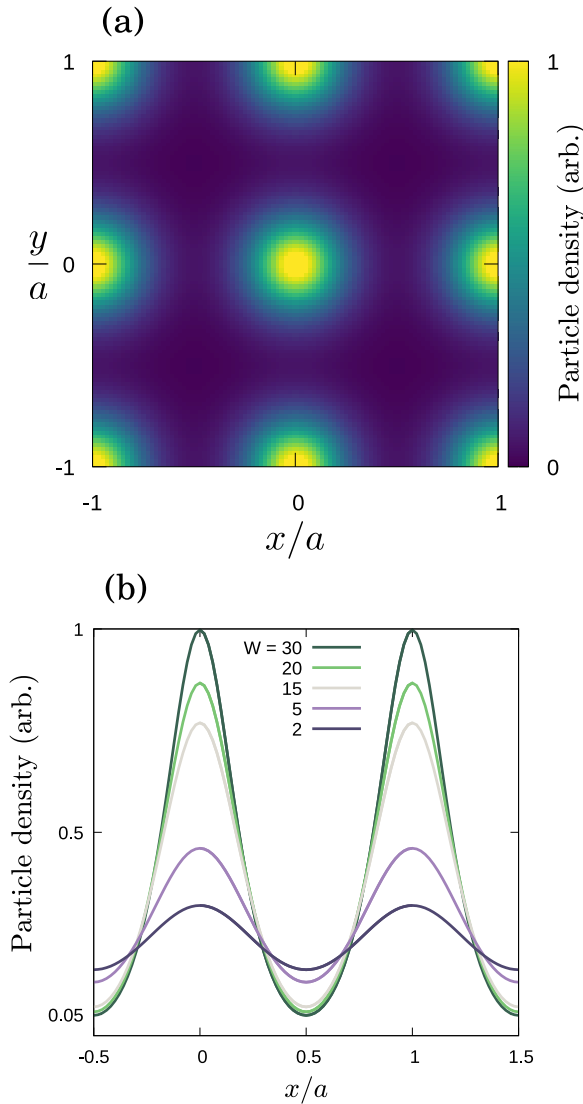
FIG. 5. Particle density of electrons in the flat band for different values W at $\Delta = 15$ meV. (a) Map of particle density at $W = 30$ meV. (b) Cuts of particle density along $y = 0$ for $W = 2$ to 30 meV.

to the square lattice by making the imposed potential sufficiently strong. We can investigate localization by computing the particle density due to the sum of all electrons within the first hole band. That is, we can compute

$$\rho_n(\boldsymbol{r}) = \sum_{\boldsymbol{k},\sigma} |\psi_{n,\boldsymbol{k},\sigma}(\boldsymbol{r})|^2,$$

where the band index is $n = -1$. Our results are plotted in Fig. 5. Figure 5(a) shows a map of the particle density for $W = 30$ meV. Here, the density is peaked at the antidot sites and has square-lattice symmetry, electrons are well localized to each site. To quantify this we present some cuts of the particle density along the nearest-neighbor line between two antidot sites for different values of W [Fig. 5(b)]. We find that as W increases the particle density at the midpoint between two sites, a measure of the wave-function overlap, decreases until, at $W = 30$ meV, it is 5% its maximum value.

This strong localization to a square lattice is the reason the dispersion reproduces that of a tight-binding model with small t ($t = 0.066$ meV); it is enabled by the presence of a finite-energy gap Δ. The localization does not increase indefinitely as you increase W: once the electron is squeezed into an area the size of the antidot, further increase of W does not increase the degree of localization. Thus, the width of the particle density peak in Fig. 5(b) is around $0.4a \approx 30$ nm $= 2$R. Because localization is limited to the size of the antidot, the effective hopping parameter t does not change any further.

Note that this explains why the dispersion in Fig. 2 is particle-hole asymmetric. Our potential (Fig. 1) has a series of well-defined maxima, which can localize particles in the hole band. The minima of the potential, which can localize particles in the electron band, arise from the Poisson factor e^{-Gz} in Eq. (2) and are thus weak. A larger value of W is required to localize particles in the electron band, compared to particles in the hole band. We thus find that a flat dispersion develops in the hole bands before it develops in the electron bands, as W is turned on. We could alternatively create a flat dispersion in the electron bands by imposing an array of dots rather than antidots: the transformation $W \mapsto -W$ flips all of the energy levels like $\varepsilon \mapsto -\varepsilon$.

IV. MAPPING TO HUBBARD MODEL

The dispersion and the particle density of the flat band suggest a mapping to a tight-binding model on a square lattice. We have already shown that the bandwidth of the flat band can be used to define an effective hopping parameter for the artificial crystal $t = 0.066$ meV. Given the particle density in Fig. 5 we can also define an effective, onsite Coulomb repulsion energy U_H. We can take the form of the particle density around a single bright dot in Fig. 5(a) and treat it as the wave function for a single electron $|\psi(\boldsymbol{r})|^2$. This has to be normalized so that there is one electron per bright dot

$$\int_{\text{cell}} d^2\boldsymbol{r} |\psi(\boldsymbol{r})|^2 = 1.$$

Having extracted the function $|\psi(\boldsymbol{r})|^2$ from Fig. 5 we can compute the effective Hubbard energy

$$U_H = \frac{e^2}{\varepsilon} \int d^2\boldsymbol{r}' d^2\boldsymbol{r} \frac{|\psi(\boldsymbol{r}')|^2 |\psi(\boldsymbol{r})|^2}{|\boldsymbol{r}' - \boldsymbol{r}|},$$

where ε is roughly the dielectric constant of the encapsulating medium, which for the purpose of estimating U_H we take to be hBN so that $\varepsilon = 4$. We find that, at $W = 30$ meV, the particle density around a single bright dot is fit by a Gaussian $|\psi(\boldsymbol{r})|^2 \propto e^{-r^2/\sigma}$ with $\sigma \approx (0.25a)^2 = 0.063a^2$. After the appropriate normalization this gives a Hubbard energy $U_H \approx 10$ meV. We thus have a dramatic ratio $U_H/t \approx 150$. Our estimate of t is essentially exact, however, the estimate of U_H is an upper limit, its value will be reduced by higher-order effects. The actual value of U_H/t will then be less than this estimate.

One factor which reduces U_H is screening by the patterned gate. Any charge in the graphene layers will induce an image charge in the patterned layer which screens the Coulomb interaction. The corresponding screening length is roughly the

distance $z \approx 10$ nm between the gate and the bilayer graphene sheet. Accounting for this effect gives the following, corrected Coulomb energy:

$$\frac{e^2}{r} - \frac{e^2}{\sqrt{r^2 + 4z^2}}.$$

Repeating the estimate with this Coulomb energy gives the reduced value $U_H \approx 5$ meV, so that the ratio with t becomes $U_H/t \approx 75$.[1] Additional effects will reduce this number further, perhaps by another 50%. What is clear from this rough estimate, however, is that the Mott regime, defined by $U_H/t \sim 7$ [34], is well within reach of experiments. In all of these estimates we have fixed the lattice constant at $a = 80$ nm. Supposing that we could scale the system down in all directions by half, so that $a = 40$ nm and $R = 7.5$ nm, we would expect $t \sim 1/a^2$ to increase by a factor 4 and $U_H \sim 1/R$ to increase by a factor 2. The scaled Hubbard ratio is then $U_H/t \sim 40$. By tuning the value of W from zero to 30 meV we can turn bilayer graphene from a weakly interacting gas of delocalized electrons to a strongly interacting, highly localized electron system.

V. OTHER LATTICE SYMMETRIES

So far we have considered only the simplest possible patterning, a square array of antidots. We have shown that electrons in bilayer graphene can be localized to antidot sites by a moderate applied potential. The obvious next step is to try other kinds of antidot arrays, and to see whether we can achieve localization on, say, triangular, kagome, or Lieb lattices. Any of these patterns are experimentally possible.

Figure 6 plots the dispersion of the flat bands for three different lattice symmetries. In each calculation we have kept the parameters identical to those in Fig. 2(c); that is, $W = 30$ meV, $\Delta = 15$ meV, and $a = 80$ nm. Figure 6(a) plots the first hole band ($n = -1$) for a triangular antidot lattice. This band replaces the single flat band in Fig. 3 that we computed for the square lattice. We find that the dispersion of the flat band matches that of a tight-binding model on a triangular lattice with nearest-neighbor hopping parameter $t = 0.067$ meV.

We can also reproduce the dispersion of a kagome lattice and a Lieb lattice. The potentials are plotted around one unit cell in the insets of Figs. 6(b) and 6(c). In these calculations we have kept the nearest-neighbor distance the same, at $a = 80$ nm, however, the overall lattice constant for these patterns is double that. Formally, the Brillouin zones in Figs. 6(b) and 6(c) are not the same as those in Figs. 6(a) and 3. Since the kagome and the Lieb patterns each have three antidot sites per unit cell, the corresponding tight-binding models each have three energy bands. In our calculation for bilayer graphene we thus expect three bands instead of one; the single, isolated flat band in Fig. 2 becomes a triplet of isolated bands in Figs. 6(b) and 6(c) whose total bandwidth is roughly the same as the single flat band in Fig. 2. We find that the dispersion
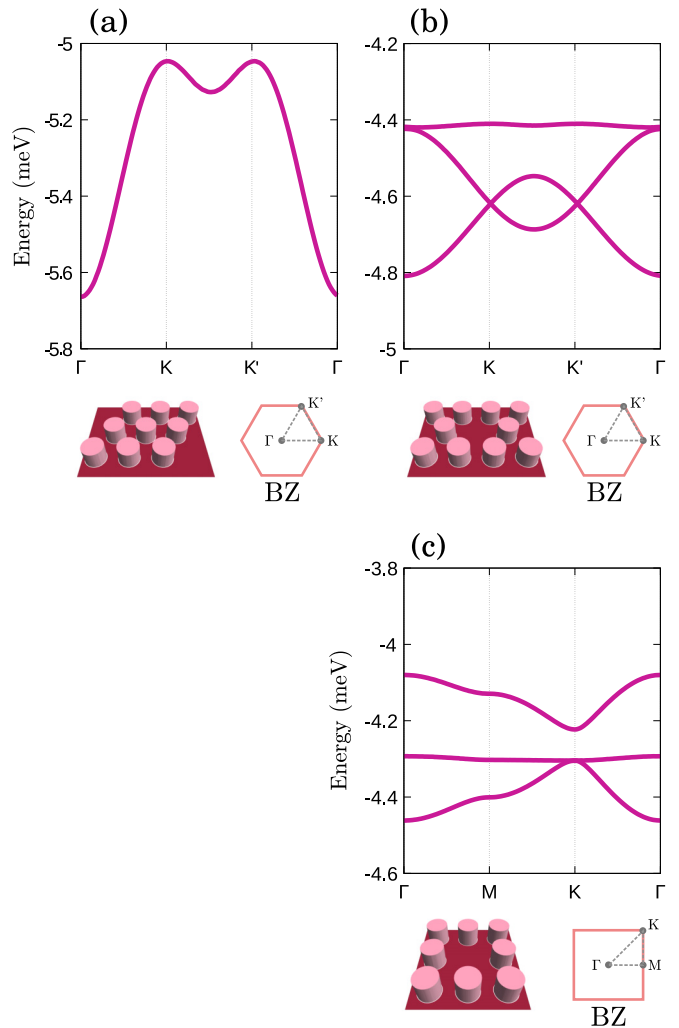
FIG. 6. Dispersion of the first holelike bands for different lattice symmetries. These replace the single, flat band in Fig. 2(c). All parameters are the same as in Fig. 2: $W = 30$ meV, $a = 80$ nm, and $\Delta = 15$ meV. (a) Band $n = -1$ for a triangular lattice potential. (b) Bands $n = -1$, -2, -3 for a kagome lattice potential. (c) Bands $n = -1$, -2, -3 for a Lieb lattice potential. Each inset plots the potential energy at the gate in real space, as well as the Brillouin zone. Vertical scale is 0.8 meV in each panel.

for a kagome antidot lattice [Fig. 6(b)] mimics that of a kagome tight-binding model with effective hopping parameter $t \approx 0.033$ meV. And the dispersion for a Lieb antidot lattice [Fig. 6(c)] matches that of a Lieb tight-binding model with the same value $t \approx 0.033$ meV. Note that these dispersions do not map perfectly onto a nearest-neighbor tight-binding model, there is an additional, small, next-nearest-neighbor hopping term t'. While t' is small it can still qualitatively change the behavior of the system [35].

In addition to these patterns one could also create an artificial honeycomb lattice. This would produce two graphenelike bands. Or, to mimic hexagonal boron nitride (hBN), one could create a honeycomb lattice with broken sublattice symmetry, for example, by giving each sublattice a different antidot radius. Given the existence of high-quality devices based on real graphene, one may ask why there is a need to engineer

---

[1]In other systems, such as twisted bilayer graphene, gate screening can drive the system below the Mott point. See Refs. [44–46]. In our case, however, the value of U_H/t is so large that even with account of gate screening the system is still above the Mott point.
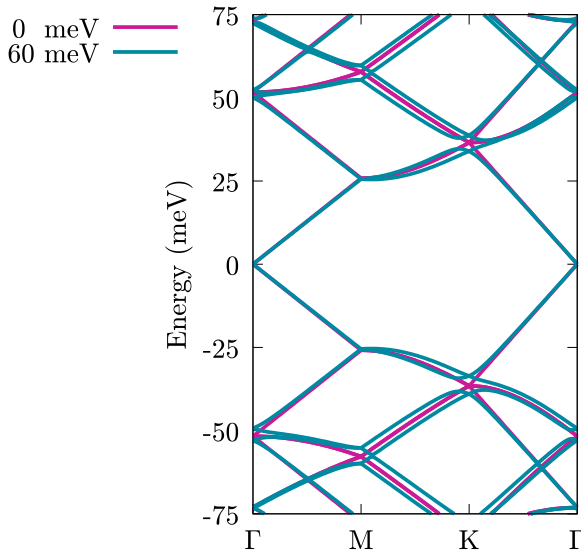
FIG. 7. Dispersion of patterned monolayer graphene for $W = 0$ and 60 meV. All other parameters are identical to those used for computing Fig. 2: $a = 80$ nm, $R = 15$ nm, and $z = 10$ nm.

artificial graphene. The artificial system gives an opportunity to study the strongly correlated regime, which does not exist in natural graphene.

VI. COMPARISON WITH PATTERNED MONOLAYER GRAPHENE

We can demonstrate that bilayer graphene is uniquely suited for this kind of artificial crystal by repeating our calculations for patterned monolayer graphene. In this case the Hamiltonian will be

$$H = \begin{bmatrix} 0 & vp_- \\ vp_+ & 0 \end{bmatrix} + U(\boldsymbol{r}),$$

which can be numerically diagonalized by almost exactly the same technique that we described in Sec. II.

The results for patterned monolayer graphene are given in Fig. 7. To be able to compare this directly with our results for bilayer graphene we have kept all parameters identical to those used for Fig. 2: the only difference is that two, stacked sheets of graphene have been replaced by one sheet only. Clearly, over the same range of W, the linear bands of monolayer graphene are not heavily reconstructed by the periodic potential. Even extending the calculation to $W = 60$ meV does not provide a significant change in the band structure. The reason for this is partly the difference in energy scales between MLG and BLG, and partly because MLG has no band gap. If K is the magnitude of momentum at the artificial Brillouin-zone vertex, then the bare MLG energy at this point is vK, and the bare BLG energy at the same point is roughly $K^2/2m^*$. To significantly restructure the energy bands the applied potential has to be larger than each of these energy scales. Since $vK \gg K^2/2m^*$, MLG requires a much larger potential strength. We have also shown that the development of the flat band in BLG is related to the band gap Δ. The fact that no such equivalent gap exists in MLG is another reason why it is difficult to localize electrons in this system.
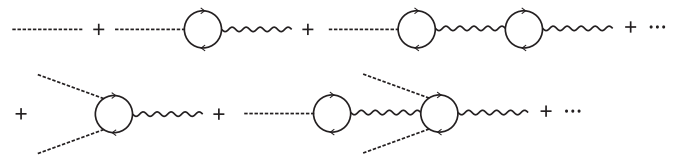
FIG. 8. Typical diagrams for screening of an external potential. The dashed line represents the external potential, the wavy line represents the electron-electron Coulomb interaction, and the solid line represents the electronic Green's function. The first line is the usual RPA summation while the second line shows some diagrams of higher order in the external potential.

VII. METHOD FOR ADDRESSING COULOMB SCREENING IN BILAYER GRAPHENE

The amplitude of the imposed (external) potential is reduced by electron-electron screening, and since our results depend on a sufficiently large potential amplitude, it is necessary to check that screening does not kill the effects described above entirely. While this issue is practically important, our approach to screening in bilayer graphene has a broader theoretical importance; the technique that we develop is applicable to bilayer graphene in general, and not just to the patterned system we focus on here.

Generally, one of two methods can be used to account for Coulomb screening of an external potential in a many-body system. These methods are (i) a brute-force Hartree or Hartree-Fock method, and (ii) a summation of screening diagrams.

The brute-force method (i) originates from atomic physics where it is widely used [36]. The method is conceptually simple and is valid for an arbitrarily strong potential, however, it requires a self-consistent procedure for *all single-electron states* from the chemical potential down to the bottom of the valence band. Within this procedure even bound states below bottom of the valence band can be important. For example, if one places a Pb atom in a strong external electric field then one needs to self-consistently recalculate all 82 electron states starting from the deepest $1s$ state. For this reason the method (i) is computationally expensive and is therefore seldom used in condensed matter physics. It has, however, been used to analyze supercritical, charged impurities in graphene [37].

The diagrammatic method (ii) is more natural theoretically but more complex conceptually. The essence of this method is the summation of all screening diagrams, some of which are shown in Fig. 8. Within this approach screening comes only from states close to the chemical potential, electron states deep in the valence band do not contribute to screening.

Screening to first-order in the external potential is described by the first line of Fig. 8. This is standard, random phase approximation (RPA) screening, the summation is easy to evaluate, and thus the method is used widely in practice. When the external potential is strong the RPA approximation is not sufficient. Multileg diagrams shown schematically in the second line of Fig. 8 become important. These diagrams can be generated from the usual RPA chain with the following electronic Green's function:

$$G = \underrightarrow{\quad} + \underrightarrow{\underset{}{\vphantom{|}}} + \cdots$$

This situation is somewhat similar to the nonlinear Heisenberg-Euler action in QED [38] (for an application to condensed matter systems, see Ref. [39]). In particular cases the summation of all diagrams beyond RPA is possible, for example, using a special technique developed in QED. Such a summation has been performed for the problem of supercritical, charged impurities in graphene [40]. This diagram summation is very involved, and for a generic potential shape the summation is practically impossible.

The purpose of this section is to develop an alternate method to account for screening of an external potential. The method is valid for an arbitrarily strong external potential, and in this sense the method is similar to method (i). On the other hand, the method does not require explicit account of very deep electron states. In this sense it is similar to method (ii). We develop the alternate method specifically for bilayer graphene, however, the method can in principle be extended to other semimetals like monolayer graphene. The method is valid for an external potential of arbitrary shape, including periodic potentials, which are of practical interest for this work, and also impurity potentials as in the subcritical or supercritical impurity problem. We consider only Hartree screening.

Before presenting the details of our method we briefly define the quantities which enter into a generic screening problem. Suppose that we have an imposed, external potential $U_0(\boldsymbol{r})$, and a self-consistent potential $\widetilde{U}(\boldsymbol{r})$, which accounts for electron-electron screening. In general, $\widetilde{U} < U_0$, and we must check, for an experimentally realistic U_0, that the corresponding $\widetilde{U}$ is capable of generating a flat band. We need to address both the shape of $\widetilde{U}(\boldsymbol{r})$ and its total amplitude. Our approach is to use the self-consistent Hartree equation

$$\widetilde{U}(\boldsymbol{q}) = U_0(\boldsymbol{q}) + \frac{2\pi e^2}{\varepsilon q} n_q,$$

$$n_q = \int e^{i\boldsymbol{q}\cdot\boldsymbol{r}} n(\boldsymbol{r}) d^2\boldsymbol{r}, \qquad (3)$$

where n_q is the Fourier amplitude for the total density of particles, a functional of $\widetilde{U}$. Fourier amplitudes of $\widetilde{U}$ and U_0 are defined similarly. This equation is just an expression of Coulombs law and is independent of the strength of the potential.

Lastly, let us quantify the meaning of weak and strong potentials. The parabolic band approximation is valid in bilayer graphene up to an energy scale about $E_p \lesssim \gamma$, where $\gamma = 380$ meV. We will use the parabolic approximation and hence assume that the self-consistent potential is smaller than this scale, $\widetilde{U} \ll E_p$. Both strong and weak potentials must satisfy this condition. Now, the potential $\widetilde{U}$ has a spatial scale: in our case this is the period of the superlattice a. The corresponding wave vector is $g \sim 2\pi/a$, and the corresponding energy scale is $E_c \sim g^2/2m^*$. For $a = 80$ nm the energy scale is $E_c \sim 10$ meV. A potential with amplitude much smaller than this value is a weak potential, and the usual RPA approximation is sufficient in this case. However, we saw in previous sections that generate a flat band one needs a potential with amplitude comparable to E_c, even somewhat larger. This is the limit of strong potential amplitude and one cannot rely on RPA in this case; an alternate method is needed to account

for screening. Note that the potential amplitude defined above W was defined at the metallic gate. The quantity we need to compare with E_c is actually $e^{-gz}W = 0.46W$, the amplitude within the graphene bilayer.

A. Description of the alternate method

The major challenge in applying Eq. (3) is to compute the particle density n_q. A complete calculation of n_q requires summation over all states from μ down to the bottom of the band, which is inaccessible in our continuum model. To resolve this issue we introduce an intermediate energy scale Λ, defined by $\max(E_c, \Delta) \ll \Lambda \ll E_p$. This scale splits the total energy range into two regions. The essence of our method is the following procedure: electronic states within the first region, $-\Lambda < \varepsilon < \mu$, are accounted for using exact numerics, and electronic states within the second region, $\varepsilon < -\Lambda$, are accounted for using exact analytics. Of course, we must check that the final result is independent of the precise value of Λ.

Note that the potential is position dependent, and that the variables μ, ε, and Λ are global, they are position independent. The position-dependent electron density can be written as

$$n(\boldsymbol{r}) = \sum_{\varepsilon_{\boldsymbol{p}} < \mu} |\psi_{\boldsymbol{p}}(\boldsymbol{r})|^2 = n_{\text{Top}}(\boldsymbol{r}) + n_{\text{Bot}}(\boldsymbol{r}),$$

$$n_{\text{Top}}(\boldsymbol{r}) = \sum_{-\Lambda < \varepsilon_{\boldsymbol{p}} < \mu} |\psi_{\boldsymbol{p}}(\boldsymbol{r})|^2, \qquad (4)$$

$$n_{\text{Bot}}(\boldsymbol{r}) = \sum_{\varepsilon_{\boldsymbol{p}} < -\Lambda} |\psi_{\boldsymbol{p}}(\boldsymbol{r})|^2,$$

where the notation n_{Top} stands for summation over states in the top part of the energy range, while n_{Bot} stands for summation over states in the bottom part of the energy range. The wave function $\psi_{\boldsymbol{p}}(\boldsymbol{r})$ is the Bloch wave calculated in the self-consistent potential $\widetilde{U}(\boldsymbol{r})$ (strictly speaking, $\boldsymbol{p}$ as it is written above must be the quasimomentum in the extended zone scheme, that is, it ranges over the entire Brillouin of the underlying graphene lattice in Fig. 1).

We can find the Bloch waves with energies $-\Lambda < \varepsilon < \mu$ numerically, using the techniques described in Sec. II. The contribution $n_{\text{Top}}(\boldsymbol{r})$ to the total charge density can thus be computed numerically. On the other hand the remaining contribution $n_{\text{Bot}}(\boldsymbol{r})$ is inaccessible to this numerical technique. We compute n_{Bot} analytically using the Thomas-Fermi approximation. This is valid at $\varepsilon_{\boldsymbol{p}} < -\Lambda$, when the electron de Broglie wavelength is much smaller than the superlattice period a. In other words, the semiclassical picture makes sense only for states with large momentum, $\varepsilon_{\boldsymbol{p}} \approx -p^2/2m^* < -\Lambda$ (where $\boldsymbol{p}$ is measured relative to a particular valley of bilayer graphene). We can thus disregard the position-momentum Heisenberg uncertainty relation and can talk about a momentum distribution at each point in space $\boldsymbol{r}$. This is shown schematically in Fig. 9.

It is obvious from Fig. 9 that the Thomas-Fermi density reaches its maximum at the potential minimum, and vice versa. In other words, the Thomas-Fermi density is exactly out of phase with $\widetilde{U}(\boldsymbol{r})$. Given that the density of states for a quadratic dispersion is energy independent, $\rho = m^*/2\pi$, we

$= n_{Bot}(r) =$ Semiclassical Contribution
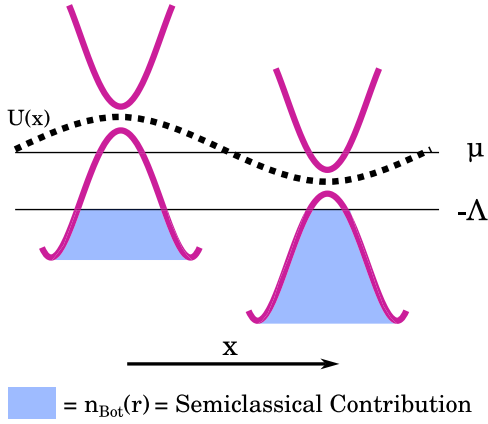
FIG. 9. Schematic illustrating the contribution to particle density from electron states deep within the BLG band. The dashed line represents the potential energy. The purple lines represent the bare, bilayer graphene dispersion. The zero of the dispersion is pinned to the potential energy, giving a position-dependent shift in the energy bands. This contribution is due to states between $-\Lambda$ and the bottom of the band, it is in antiphase with the potential and can be described within the Thomas-Fermi approximation.

can write the total particle density due to states below $-\Lambda$ as

$$n_{\text{Bot}}(\boldsymbol{r}) = \sum_{\varepsilon_{\boldsymbol{p}} < -\Lambda} |\psi_{\boldsymbol{p}}(\boldsymbol{r})|^2 = -4\rho\widetilde{U}(\boldsymbol{r}) = -\frac{2m^*}{\pi}\widetilde{U}(\boldsymbol{r}). \quad (5)$$

The factor 4 comes from spin and valley degeneracy. Equations (4) and (5) summarize our method. Interestingly, n_{Bot} is independent of Λ.

B. Testing the alternate method against RPA

The alternate method is valid for for any potential with amplitude $U \ll E_p$. Of course, it is also valid in the limit $U \ll E_c$, where RPA can be applied. The purpose of this section is to compare the results of the alternate method with those of RPA and to show that the two methods agree in the limit of weak potential. Of course, this alternate method can be applied beyond this limit. To do so we consider the simplest possible situation: bilayer graphene at the charge-neutrality point ($\mu = 0$) with an exactly parabolic dispersion ($\varepsilon = \pm p^2/2m^*$). We also assume a simpler form for the screened potential, taking only two Fourier components

$$\widetilde{U}(\boldsymbol{r}) = 2\widetilde{W}[\cos(gx) + \cos(gy)]. \quad (6)$$

As before, the period of the superlattice is 80 nm and $g = 2\pi/a$. We will articulate our answer in terms of $\widetilde{W}$, considering the range $0 < \widetilde{W} < 1$ meV where RPA is valid, and also the range $W > 1$ meV, where RPA breaks down. The particle density is a functional of the potential in Eq. (6) and can be computed using either the alternate method or using RPA.

Let us first recall the textbook results of RPA theory. Suppose that a probe charge with density $\rho(\boldsymbol{r})$ is added to the system. The probe charge interacts both with the external potential and with the particle density $n(\boldsymbol{r})$ of electrons in the filled Dirac sea. This interaction energy and its corresponding

diagram chain are given by

$$\widetilde{U}_q\rho_q = U_q^0\rho_q + \frac{2\pi e^2}{\varepsilon q}n_q\rho_q$$

$$\qquad\qquad (7)$$

As in Fig. 8, the dashed line represents the external potential U_q^0, the solid line represents the electronic Green's function, the wavy line represents the Coulomb interaction, and the black dot represents the probe charge. Since $U_q^0\rho_q$ corresponds to the first diagram in Eq. (7), the remaining diagrams can be summed to obtain an expression for $(2\pi e^2/\varepsilon q)n_q\rho_q$. We find that

$$\frac{2\pi e^2}{\varepsilon q}n_q\rho_q = U_q^0\Pi_q\frac{1}{1 - \frac{2\pi e^2}{\varepsilon q}\Pi_q}\frac{2\pi e^2}{\varepsilon q}\rho_q, \quad (8)$$

where Π_q is the static polarization operator, corresponding to the electron loop in Eq. (7). Hence,

$$n_q = n_{\text{RPA}}(q) = \frac{U_q^0}{1 - \frac{2\pi e^2}{\varepsilon q}\Pi_q}\Pi_q = \widetilde{U}_q\Pi_q. \quad (9)$$

This is the general RPA expression for induced electron density. For unbiased bilayer graphene the polarization operator is independent of q [41]:

$$\Pi_q = -2\ln(4)\frac{m^*}{\pi}. \quad (10)$$

For biased bilayer graphene ($\Delta > 0$) the polarization operator is q dependent and must be evaluated at $q = g$ [because $\widetilde{U}_q$ in Eq. (9) is nonzero only for $q = g$]. This calculation has been performed, for example, in Ref. [42] and we make use the general expression for Π_q in that work to find Π_g at $\Delta = 5$ meV and at $\Delta = 15$ meV. Equations (7), (9), and (10) solve the RPA screening problem.

For the potential in Eq. (6) the induced RPA density is of exactly the same shape as $\widetilde{U}(\boldsymbol{r})$:

$$n_{\text{RPA}}(\boldsymbol{r}) = -2n_0[\cos(gx) + \cos(gy)]. \quad (11)$$

The total variation in charge density from maximum to minimum is given by $\delta n_{\text{RPA}} = 8n_0$. We find that the charge density $n_{\text{Top}}(\boldsymbol{r}) + n_{\text{Bot}}(\boldsymbol{r})$, computed using our method is also sinusoidal. It is thus possible to compare RPA with our method by comparing the values of δn. This comparison is given in Fig. 10, for the sake of clarity we plot $\delta n/\widetilde{W}$ versus $\widetilde{W}$ (rather than δn itself). We plot this comparison at $\Delta = 0$ [Fig. 10(a)], $\Delta = 5$ meV [Fig. 10(b)], and $\Delta = 15$ meV [Fig. 10(c)]. In each panel we plot the RPA result $\delta n_{\text{RPA}}/\widetilde{W}$ (pink line), and the result of our alternate method $\delta n_{\text{Top+Bot}}/\widetilde{W}$ (green line). As expected, the two methods are in exact agreement when the potential is weak ($\widetilde{W} \lesssim 1$ meV). The RPA result deviates from the result of our alternate method at larger values of $\widetilde{W}$, when the assumptions of RPA theory become invalid. Note that our alternate method is applicable for all values of $\widetilde{W}$.

(a) $\Delta = 0$ meV

(b) $\Delta = 5$ meV

(c) $\Delta = 15$ meV

δn_{RPA}

$\delta n_{(Top+Bot)}$

δn_{Bot}
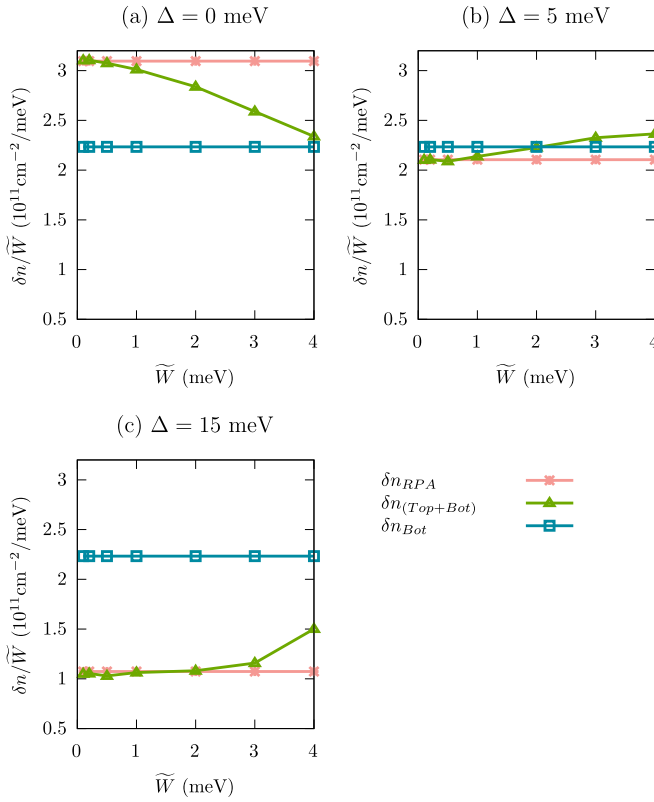
FIG. 10. Comparison between two calculations of the total variation in particle density at (a) $\Delta = 0$, (b) $\Delta = 5$ meV, and (c) $\Delta = 15$ meV. In each panel the pink curve is the RPA result $\delta n_{RPA}/\widetilde{W}$, the green curve is result of the alternate method $\delta n_{Top+Bot}/\widetilde{W}$, and the blue curve is the contribution of just the deep electron states $\delta n_{Bot}/\widetilde{W}$.

In Fig. 10 we also present the contribution to the total particle density from deep electron states $\delta n_{Bot}/\widetilde{W}$ (blue line). From Eq. (5) we expect $\delta n_{Bot}/\widetilde{W}$ to be constant. Figure 10 shows that n_{Bot} gives the major contribution to particle density. The contribution due to states near the chemical potential n_{Top} is at most 50% of the total and can even become zero [when the green line intersects the blue line in Figs. 10(a) and 10(b)]. The situation in RPA theory is the opposite: spatial variation in particle density comes exclusively from states near the chemical potential.

Lastly, note the sign of the particle density. Both $n_{RPA}(\boldsymbol{r})$ and $n_{Bot}(\boldsymbol{r})$ have a sign opposite to that of $\widetilde{U}(\boldsymbol{r})$ [see Eqs. (5) and (9)]. The remaining term $n_{Top}(\boldsymbol{r})$ can have either sign. If δn_{RPA} is larger than δn_{Bot} then $n_{Top}(\boldsymbol{r})$ has a sign opposite to $\widetilde{U}(\boldsymbol{r})$ [this is the case in Fig. 10(a)]. On the other hand, if δn_{RPA} is smaller than δn_{Bot}, then $n_{Top}(\boldsymbol{r})$ has the same sign as $\widetilde{U}(\boldsymbol{r})$ [this is the case in Figs. 10(a) and 10(b)]. The sign of $n_{Top}(\boldsymbol{r})$ can be positive or negative [relative to $\widetilde{U}(\boldsymbol{r})$] and can change as a function of $\widetilde{W}$. The sign of the total charge density $n_{Top}(\boldsymbol{r}) + n_{Bot}(\boldsymbol{r})$ is, however, always opposite to $\widetilde{U}(\boldsymbol{r})$.

C. Hartree screening in the flat-band limit

Having established that the particle density can be computed using Eqs. (4) and (5) we can now compute $n(\boldsymbol{r})$ for the flat-band system shown in Fig. 2(c). This allows us to find the relationship between U_0 and $\widetilde{U}$ via the Hartree equa-

tion [Eq. (3)]. We will work under the assumption that an applied potential U_0 will maintain the same shape after screening has been accounted for, that is, $\widetilde{U}(\boldsymbol{r})$ differs from $U_0(\boldsymbol{r})$ by a constant scaling factor. Our goal is to estimate this scaling factor, which corresponds to a reduction in the effective value of W. To show that this assumption is reasonable we solve the Hartree equation in reverse. First, suppose that $\widetilde{U}(\boldsymbol{r})$ has exactly the same form as the potential energy defined by Eq. (2); its amplitude is $W \mapsto \widetilde{W}$. We take this as an ansatz solution to the Hartree equation. Given the form of $\widetilde{U}(\boldsymbol{r})$ we can compute $U_0(\boldsymbol{r})$ using the Hartree equation

$$U_0(\boldsymbol{r}) = \widetilde{U}(\boldsymbol{r}) - \int \frac{e^2}{\varepsilon|\boldsymbol{r} - \boldsymbol{r}'|} n(\boldsymbol{r}') d^2\boldsymbol{r}',$$

where $n(\boldsymbol{r})$ is a functional of $\widetilde{U}(\boldsymbol{r})$ given by Eqs. (4) and (5). If this form for $\widetilde{U}(\boldsymbol{r})$ is correct, then $U_0(\boldsymbol{r})$ computed using the above equation will have the same form as the original potential; that is, $U_0(\boldsymbol{r})$ will differ from $\widetilde{U}(\boldsymbol{r})$ by a multiplicative factor. We can then characterize the strength of screening in bilayer graphene by estimating this factor.

Indeed, computing $U_0(\boldsymbol{r})$ in this way gives a function which is essentially of the same form as $\widetilde{U}(\boldsymbol{r})$. We present a comparison of these two functions in Fig. 11 for $\widetilde{W} = 30$ meV and for μ at the charge-neutrality point (filling fraction $f = 0$). In the first panel, which is a cut of both functions along $y = 0$, we find that the two functions are identical up to a scaling factor 4.3. In the second panel, a cut along $y = a/2$ using the same scaling factor, the two functions are roughly equivalent except for the structure of their minima. We conclude that screening has only a small effect on the shape of the potential, and that its main effect is to scale the amplitude of the potential by a constant factor.

We can now estimate the strength of electron-electron screening in patterned bilayer graphene. We focus on two points of interest: (i) the charge-neutrality point (complete filling of the flat band) and (ii) the Mott point (one-quarter-filling of the flat band, or one electron per antidot site). These correspond, respectively, to the point of weakest screening and to the point of strongest screening (as far as experimentally interesting points within the flat band go). Note that typically the Mott point occurs at half-filling of a band. Here, because the system is both valley and spin degenerate, we must consider quarter-filling (that is, a filling fraction $f = -3n_0/4$). At these two filling fractions we fix the self-consistent potential amplitude $\widetilde{W}$ and compute the amplitude W_0 that the applied potential must have to achieve this value of $\widetilde{W}$.

Our results are given in Fig. 12. At the charge-neutrality point (purple curve) we find that W_0 is consistently around 4.3 times larger than $\widetilde{W}$. This means that the effect of screening is to reduce the applied potential by a factor ≈ 4.3. At the Mott point (blue curve) screening is stronger: to achieve $\widetilde{W} = 30$ meV an applied potential $W_0 \approx 8.3\widetilde{W}$ is required. As the electron density is tuned into the flat band the influence of an applied potential becomes weaker, and the amplitude of this potential needs to be increased to maintain the flat band.

The stronger screening at $f = -3n_0/4$ can be understood in terms of the particle density within the flat band that was presented in Fig. 5. The major contribution to the spatial variation of $n_{Top}(\boldsymbol{r})$ comes from the flat band. This

Cut along y=0
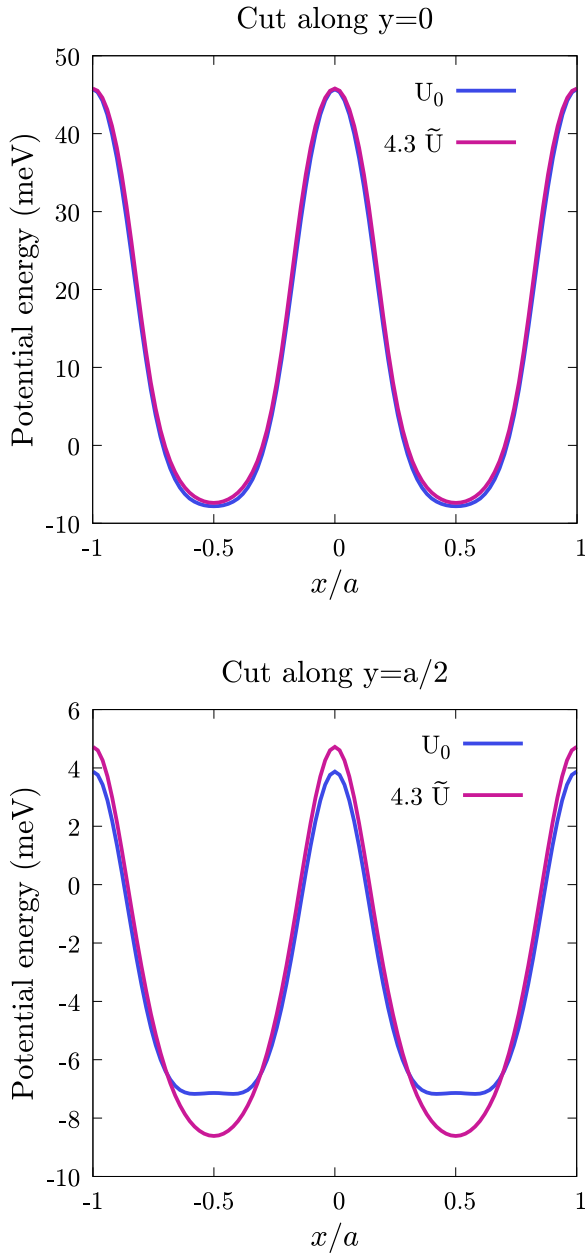
Cut along y=a/2

FIG. 11. Plot of $\widetilde{U}(\mathbf{r})$, defined by Eq. (2) with $\widetilde{W} = 30$ meV (purple line). Also shown is the function $U_0(\mathbf{r})$ (blue line) consistent with the Hartree equation [Eq. (3)]. In the first panel the cut has been taken along $y = 0$, and in the second panel the cut is along $y = a/2$. In both panels $\widetilde{U}$ has been scaled by a factor 4.3.

FIG. 12. Applied potential strength W_0 as a function of the self-consistent potential strength $\widetilde{W}$ for two different filling fractions f. A filling fraction $f = 0$ corresponds to the charge neutrality point and a filling fraction of $f = -3n_0/4$, or one-quarter -illing of the flat band, corresponds to the Mott point.

to be $z = 10$ nm. then the maximum potential amplitude is 7 eV, well above the value $W_0 = 250$ meV required for a fully developed flat band at the point of strongest screening.

VIII. CONCLUSIONS

We have suggested a simple method for generating a flat band in bilayer graphene. Within this flat band we find the following: (i) Bilayer graphene can be driven into the strongly correlated regime by application of a band gap and long-wavelength, periodic electric field. (ii) The strongly correlated regime can be accessed by either tuning the band gap or the amplitude of the periodic modulation, keeping electron density fixed. (iii) We present a general technique for addressing Hartree screening in bilayer graphene. While this technique has more broad theoretical applications, we use it to verify that electron-electron screening of the periodic potential is not strong enough to destroy the effects listed above. (iv) Patterned bilayer graphene can mimic the dispersions of a variety of different two-dimensional lattices, including square, triangular, kagome, and Lieb lattices. By appropriate patterning it is possible to design the underlying effective Hubbard model.

contribution is in phase with the potential, meaning that its sign is opposite to that of $n_{\text{Bot}}(\mathbf{r})$. It thus acts to reduce the strength of the screening. If we then move μ to the Mott point we remove a majority of these electrons, which are in phase with the potential, leading to an increase in the strength of screening.

While the estimate given here is rough, it gives an idea of the strength of screening in these systems. In particular it shows that $\widetilde{W} = 30$ meV is well within reach of experiments. A PBG device using hBN as a substrate has a breakdown field of 0.7 Vn^{-1}m [43]. If we take the thickness of hBN

[1] Y. Cao, V. Fatemi, S. Fang, K. Watanabe, T. Taniguchi, E. Kaxiras, and P. Jarillo-Herrero, Nature (London) **556**, 43 (2018).

[2] R. Bistritzer and A. H. MacDonald, Proc. Natl. Acad. Sci. USA **108**, 12233 (2011).

[3] X. Lu, P. Stepanov, W. Yang, M. Xie, M. A. Aamir, I. Das, C. Urgell, K. Watanabe, T. Taniguchi, G. Zhang *et al.*, Nature (London) **574**, 653 (2019).

[4] M. Yankowitz, S. Chen, H. Polshyn, Y. Zhang, K. Watanabe, T. Taniguchi, D. Graf, A. F. Young, and C. R. Dean, Science **363**, 1059 (2019).

[5] G. Chen, A. L. Sharpe, P. Gallagher, I. T. Rosen, E. J. Fox, L. Jiang, B. Lyu, H. Li, K. Watanabe, T. Taniguchi *et al.*, Nature (London) **572**, 215 (2019).

[6] J. M. Park, Y. Cao, K. Watanabe, T. Taniguchi, and P. Jarillo-Herrero, Nature (London) **590**, 249 (2021).

[7] Y. Cao, V. Fatemi, A. Demir, S. Fang, S. L. Tomarken, J. Y. Luo, J. D. Sanchez-Yamagishi, K. Watanabe, T. Taniguchi, E. Kaxiras *et al.*, Nature (London) **556**, 80 (2018).

[8] A. Kerelsky, L. J. McGilly, D. M. Kennes, L. Xian, M. Yankowitz, S. Chen, K. Watanabe, T. Taniguchi, J. Hone, C. Dean *et al.*, Nature (London) **572**, 95 (2019).

[9] G. Chen, L. Jiang, S. Wu, B. Lyu, H. Li, B. L. Chittari, K. Watanabe, T. Taniguchi, Z. Shi, J. Jung *et al.*, Nat. Phys. **15**, 237 (2019).

[10] A. L. Sharpe, E. J. Fox, A. W. Barnard, J. Finney, K. Watanabe, T. Taniguchi, M. A. Kastner, and D. Goldhaber-Gordon, Science **365**, 605 (2019).

[11] M. Serlin, C. L. Tschirhart, H. Polshyn, Y. Zhang, J. Zhu, K. Watanabe, T. Taniguchi, L. Balents, and A. F. Young, Science **367**, 900 (2020).

[12] Y. Jiang, X. Lai, K. Watanabe, T. Taniguchi, K. Haule, J. Mao, and E. Y. Andrei, Nature (London) **573**, 91 (2019).

[13] C. Rubio-Verdú, S. Turkel, Y. Song, L. Klebl, R. Samajdar, M. S. Scheurer, J. W. F. Venderbos, K. Watanabe, T. Taniguchi, H. Ochoa *et al.*, Nat. Phys. **18**, 196 (2022).

[14] Z. Zhang, Y. Wang, K. Watanabe, T. Taniguchi, K. Ueno, E. Tutuc, and B. J. LeRoy, Nat. Phys. **16**, 1093 (2020).

[15] Z. Lin, J.-H. Choi, Q. Zhang, W. Qin, S. Yi, P. Wang, L. Li, Y. Wang, H. Zhang, Z. Sun *et al.*, Phys. Rev. Lett. **121**, 096401 (2018).

[16] B. R. Ortiz, S. M. L. Teicher, Y. Hu, J. L. Zuo, P. M. Sarte, E. C. Schueller, A. M. Milinda Abeykoon, M. J. Krogstad, S. Rosenkranz, R. Osborn, R. Seshadri, L. Balents, J. He, and S. D. Wilson, Phys. Rev. Lett. **125**, 247002 (2020).

[17] B. R. Ortiz, P. M. Sarte, E. M. Kenney, M. J. Graf, S. M. L. Teicher, R. Seshadri, and S. D. Wilson, Phys. Rev. Mater. **5**, 034801 (2021).

[18] K. Y. Chen, N. N. Wang, Q. W. Yin, Y. H. Gu, K. Jiang, Z. J. Tu, C. S. Gong, Y. Uwatoko, J. P. Sun, H. C. Lei, J. P. Hu, and J. G. Cheng, Phys. Rev. Lett. **126**, 247001 (2021).

[19] C. C. Zhu, X. F. Yang, W. Xia, Q. W. Yin, L. S. Wang, C. C. Zhao, D. Z. Dai, C. P. Tu, B. Q. Song, Z. C. Tao *et al.*, Phys. Rev. B **105**, 094507 (2022).

[20] Y.-X. Jiang, J.-X. Yin, M. M. Denner, N. Shumiya, B. R. Ortiz, G. Xu, Z. Guguchia, J. He, M. S. Hossain, X. Liu *et al.*, Nat. Mater. **20**, 1353 (2021).

[21] Z. E. Krix, H. D. Scammell, and O. P. Sushkov, Phys. Rev. B **105**, 075120 (2022).

[22] A. Uri, S. Grover, Y. Cao, J. A. Crosse, K. Bagani, D. Rodan-Legrain, Y. Myasoedov, K. Watanabe, T. Taniguchi, P. Moon *et al.*, Nature (London) **581**, 47 (2020).

[23] J. H. Wilson, Y. Fu, S. Das Sarma, and J. H. Pixley, Phys. Rev. Res. **2**, 023325 (2020).

[24] M. Polini, F. Guinea, M. Lewenstein, H. C. Manoharan, and V. Pellegrini, Nat. Nanotechnol. **8**, 625 (2013).

[25] R. Huber, M.-H. Liu, S.-C. Chen, M. Drienovsky, A. Sandner, K. Watanabe, T. Taniguchi, K. Richter, D. Weiss, and J. Eroms, Nano Lett. **20**, 8046 (2020).

[26] D. Q. Wang, D. Reuter, A. D. Wieck, A. R. Hamilton, and O. Klochan, Appl. Phys. Lett. **117**, 032102 (2020).

[27] D. Q. Wang, Z. Krix, O. P. Sushkov, I. Farrer, D. A. Ritchie, A. R. Hamilton, and O. Klochan, Nano Lett. **23**, 1705 (2023).

[28] S. Carr, S. Fang, P. Jarillo-Herrero, and E. Kaxiras, Phys. Rev. B **98**, 085144 (2018).

[29] J. A. Fürst, J. G. Pedersen, C. Flindt, N. A. Mortensen, M. Brandbyge, T. G. Pedersen, and A.-P. Jauho, New J. Phys. **11**, 095020 (2009).

[30] R. Huber, M.-N. Steffen, M. Drienovsky, A. Sandner, K. Watanabe, T. Taniguchi, D. Pfannkuche, D. Weiss, and J. Eroms, Nat. Commun. **13**, 2856 (2022).

[31] S. A. A. Ghorashi, A. Dunbrack, J. Sun, X. Du, and J. Cano, arXiv:2206.13501.

[32] Y. Zhang, T.-T. Tang, C. Girit, Z. Hao, M. C. Martin, A. Zettl, M. F. Crommie, Y. R. Shen, and F. Wang, Nature (London) **459**, 820 (2009).

[33] E. McCann and M. Koshino, Rep. Prog. Phys. **76**, 056503 (2013).

[34] J. Hubbard and B. H. Flowers, Proc. R. Soc. London A **281**, 401 (1964).

[35] A. Eberlein and W. Metzner, Phys. Rev. B **89**, 035126 (2014).

[36] V. A. Dzuba, V. V. Flambaum, P. G. Silvestrov, and O. P. Sushkov, Phys. Lett. A **118**, 177 (1986).

[37] V. M. Pereira, J. Nilsson, and A. H. Castro Neto, Phys. Rev. Lett. **99**, 166802 (2007).

[38] W. Heisenberg and H. Euler, Z. Phys. **98**, 714 (1936).

[39] A. C. Keser, Y. Lyanda-Geller, and O. P. Sushkov, Phys. Rev. Lett. **128**, 066402 (2022).

[40] I. S. Terekhov, A. I. Milstein, V. N. Kotov, and O. P. Sushkov, Phys. Rev. Lett. **100**, 076803 (2008).

[41] E. H. Hwang and S. Das Sarma, Phys. Rev. Lett. **101**, 156802 (2008).

[42] H. D. Scammell and O. P. Sushkov, Phys. Rev. B **107**, 085104 (2023).

[43] C. R. Dean, A. F. Young, I. Meric, C. Lee, L. Wang, S. Sorgenfrei, K. Watanabe, T. Taniguchi, P. Kim, K. L. Shepard *et al.*, Nat. Nanotechnol. **5**, 722 (2010).

[44] Z. A. H. Goodwin, V. Vitale, F. Corsetti, D. K. Efetov, A. A. Mostofi, and J. Lischner, Phys. Rev. B **101**, 165110 (2020).

[45] Y. Saito, J. Ge, K. Watanabe, T. Taniguchi, and A. F. Young, Nat. Phys. **16**, 926 (2020).

[46] P. Stepanov, I. Das, X. Lu, A. Fahimniya, K. Watanabe, T. Taniguchi, F. H. L. Koppens, J. Lischner, L. Levitov, and D. K. Efetov, Nature (London) **583**, 375 (2020).